ELSEVIER

Journal of Crystal Growth 210 (2000) 683–693

JOURNAL OF CRYSTAL GROWTH

www.elsevier.nl/locate/jcrysgro

Growth of Cr : $LiCaAlF_6$ and Cr : $LiSrAlF_6$ by the Czochralski method

D. Klimm[a,*], G. Lacayo[a,b], P. Reiche[a]

[a] *Institut für Kristallzüchtung, Max-Born-Str. 2, D-12489 Berlin, Germany*

[b] *Physikalisches Institut, AG Kristallographie, Humboldt-Universität zu Berlin, Invalidenstraße 110, D-10115 Berlin, Germany*

Received 9 November 1999; accepted 20 November 1999

Communicated by R.S. Feigelson

Abstract

Single crystals of chromium-doped LiCAF and LiSAF can be grown from nearly stoichiometric melts of the components LiF, AlF_3, CrF_3 and CaF_2 or SrF_2, respectively, by the Czochralski method. The optical quality of LiSAF crystals is usually better, as LiCAF contains more scattering particles. This different behavior can be attributed to different thermodynamic properties of both substances: The higher melting point of LiCAF leads to higher evaporation losses of volatile LiF and AlF_3. Moreover, LiCAF melts incongruently. The main problem during the growth and application of LiSAF crystals is the highly anisotropic thermal expansion that may lead to thermal cracking. The extreme hygroscopicity of the doping agent CrF_3 has to be considered for the growth of both substances.

PACS: 42.70.Hj; 81.10.Fq; 81.70.Pq

Keywords: Laser materials; Growth from melts; Thermal analysis (DTA)

1. Introduction

Already in 1971 Viebahn [1] described the trigonal structure of hexafluoroaluminates having the general formula $LiMe^{II}Me^{III}F_6$ (Me^{II} = Ca, Sr, Cd; Me^{III} = Al, Ga, Ti, V, Cr, Fe). Later Walenta et al. [2] reported on a fluoride mineral with the chemical composition $LiCaAlF_6$ that was discovered in the Bolivian tin mine Colquiri. Recently some colquiriites (named after that location) like $LiCaAlF_6$ (LiCAF) [3], $LiSrAlF_6$ (LiSAF) [4], $LiSr_{0.8}Ca_{0.2}AlF_6$ (LiSCAF) [5], $LiSrGaF_6$ (LiSGaF) [6–8] and $LiCaGaF_6$ [9] were recognized as potential host crystals for solid-state lasers. These laser materials can be pumped by diodes and conventional flashlamps and are widely tunable (LiSAF: 780 to 1010 nm [10]).

Most authors are doping the colquiriite crystals with Cr^{3+} as active ion, but Ce^{3+} is for possible ultraviolet applications [11]. The concentration of chromium present in the colquiriite-type crystals that were grown by different methods was found to be lower than within the melt. It is not possible to attribute this observation to a distribution

* Corresponding author. Tel.: + 49-30-6392-3024.

E-mail address: klimm@ikz-berlin.de (D. Klimm)

0022-0248/00/$ - see front matter
PII: S0022-0248(99)00762-9

coefficient $k_{\mathrm{eff}} = [\mathrm{Cr}]_{\mathrm{sol}}/[\mathrm{Cr}]_{\mathrm{liqu}} < 1$, as — within the range of accuracy — the solidus concentration of chromium $[\mathrm{Cr}]_{\mathrm{sol}}$ was observed to be constant along the growth axis of the boule. The explanation given in Ref. [3], that the doping agent CrF_3 evaporates is suspect too, as at least during the long-Czochralski growth process of typically 5 days $[\mathrm{Cr}]_{\mathrm{liqu}}$ should reduce continuously, leading to a monotonous drop of $[\mathrm{Cr}]_{\mathrm{sol}}$. It must be assumed, that the partial hydrolysis of CrF_3 with traces of moisture being present in the growth atmosphere and in the starting materials is responsible for the reduced incorporation of Cr^{3+} within the crystals (Section 2.2).

One crucial problem with the growth of high-quality colquiriite crystals for laser applications are scattering centers that can be found within the pulled crystals. In TEM samples prepared by ion beam thinning, these needles of typically $5 \times 5 \times 35\ \mu m^3$ were observed to have an excess of calcium: The molar concentration ratio [Ca]/[Al] ≈ 1.86 within the needles is higher as compared to the theoretical value [Ca]/[Al] = 1.00 for $LiCaAlF_6$. This observation leads to the conclusion, that the needles might consist of Ca_2AlF_7. However, attempts to observe this orthorhombic substance by diffraction patterns of electrons [12] or synchrotron radiation [13] have failed.

Unfortunately, the EDX analysis performed in Ref. [14] did not allow to determine [Li] within the needles directly. But at least the concentrations of the heavier atoms and of fluorine could be measured semiquantitatively and indicate (beyond the already mentioned excess of calcium) an increased [Ca] + [Al] + [Cr] concentration. The theoretical values for this heavy cationatomic concentration are $x_{\mathrm{hc}}^{\mathrm{th}} = 0.25 = (1+1)/(1+1+6) = 1/(1+3)$ for $LiCaAlF_6$ and AlF_3, respectively, and $x_{\mathrm{hc}}^{\mathrm{th}} = 0.33 = 1/(1+2)$ for CaF_2. For the $LiCaAlF_6$ matrix a value $x_{\mathrm{hc}}^{\mathrm{meas}} = 0.33$ was measured. Obviously, EDX overestimates $x_{\mathrm{hc}}^{\mathrm{meas}}$ by about one quarter, as a part of the volatile LiF/AlF_3 evaporates during the TEM sample preparation. From the EDX measurements $x_{\mathrm{hc}}^{\mathrm{meas}} \approx 0.39$ can be estimated for the needles. Together with the above-mentioned calcium excess this very high value indicated, that CaF_2 is enriched within the needles.

Table 1
Thermomechanical properties of LiCAF [15] and LiSAF [16] in comparison with $Y_3Al_5O_{12}$ (YAG) (*Note*: κ thermal conductivity, α – thermal expansion, K_{IC} – fracture toughness)

	LiCAF	LiSAF	YAG
κ_{11} [W/(K m)]	4.58		6.0
κ_{33} [W/(K m)]	5.14	3.09	—
α_{11} ($10^{-6}K^{-1}$)	22.0	18.8	6.7
α_{33} ($10^{-6}K^{-1}$)	3.6	−10.0	—
K_{IC} (MPa $\sqrt{\mathrm{m}}$)	0.18–0.37	0.40	1.4

2. Thermomechanical and chemical properties

2.1. Thermal expansion

Some thermomechanical properties of LiCAF and LiSAF that are important for the process of crystal pulling from the melt and for laser applications with high input of pumping energy are found in Refs. [15,16] and will be given in Table 1.

Both fluorides are much more sensitive with respect to thermal and mechanical shocks if one compares them with YAG as one other common laser material. Thermal gradients that arise either during the pulling process or during the operation of the laser can flatten only slowly due to the low thermal conductivity κ. Moreover, the coefficient of thermal expansion α is isotropic for the cubic garnet, whereas for the trigonal colquiriites this property is represented by a tensor of the order 2. The difference between α_{11} ($\perp \boldsymbol{c}$) and α_{33} ($\| \boldsymbol{c}$) is large for both LiCAF and LiSAF. Upon heating LiSAF even exhibits thermal expansion along $\boldsymbol{a}$ and thermal contraction along $\boldsymbol{c}$ (Fig. 1).

In uniform temperature fields all homogeneous bodies, isotropic or not, expand freely as due to

$$\mathrm{Inc}({}^4\bar{\boldsymbol{s}} : {}^2\bar{\boldsymbol{\sigma}}) = \mathrm{Inc}({}^2\bar{\boldsymbol{\alpha}}\Delta T) = 0. \quad (1)$$

The body is free from thermal stresses [17]. For a quantitative description of thermal stresses the components of the tensors of elastic compliance ${}^4\bar{\boldsymbol{s}}$ and of thermal expansion ${}^2\bar{\boldsymbol{\alpha}}$ should be known. The condition $\mathrm{Inc}({}^2\bar{\boldsymbol{\alpha}}\Delta T) \neq 0$ is not only necessary but also sufficient for the development of temperature stresses. Unfortunately, most components of

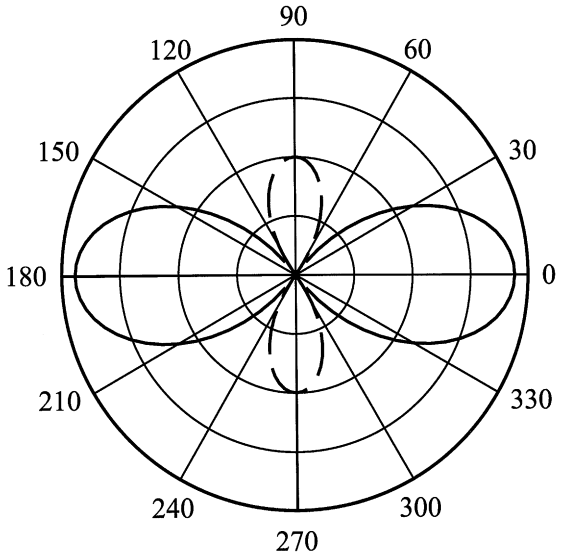

Fig. 1. Section through the representation surface for the thermal expansion index of LiSAF. $\boldsymbol{a} = 0$; $\boldsymbol{c} = 90$ (degrees). Negative values = dashed lines. One grid circle corresponds to $5 \times 10^{-6}\,\mathrm{K}^{-1}$.

${}^4\bar{\mathbf{s}}$ are unknown for $LiSrAlF_6$ (in contrast to $LiCaAlF_6$ [15]).

The components of the incompatibility tensor $\mathrm{Inc}({}^2\bar{\boldsymbol{\alpha}}\Delta T)$ can be expected to grow with the nonlinearity of the temperature gradient $\partial^2 T/\partial x_i^2$ (x_i — coordinates) [18] or with the anisotropy of the thermal expansion. If one chooses a Cartesian coordinate system (the common physical system) $\boldsymbol{e}_i$ ($i = 1, 2, 3$) such, that $\boldsymbol{e}_1 \| \boldsymbol{a}$ and $\boldsymbol{e}_3 \| \boldsymbol{c}$ of the crystallographic system [18], then the value of the thermal expansion $\alpha[n_1, n_2, n_3]$ in any arbitrary direction $\boldsymbol{n} = n_1\boldsymbol{e}_1 + n_2\boldsymbol{e}_2 + n_3\boldsymbol{e}_3$ of the trigonal crystal can be obtained from the tensor components α_{11} and α_{33} (cf. Table 1) by the scalar product

$$\alpha[\boldsymbol{n}] = \boldsymbol{n} \cdot {}^2\bar{\boldsymbol{\alpha}} \cdot \boldsymbol{n}, \tag{2}$$

which gives values that were displayed in Fig. 1 in the system of the polar coordinates $r = \sqrt{n_1^2 + n_3^2}$ and $\varphi = \arctan[n_3/n_1]$. The representation surface of the second-rank tensor ${}^2\bar{\boldsymbol{\alpha}}$ has rotational symmetry around the $\boldsymbol{e}_3 (= \boldsymbol{c})$ axis.

An analytic expression for $\alpha[\boldsymbol{n}]$ and its derivatives can be obtained by insertion of unit radius vectors $\boldsymbol{n} = [\cos\varphi, 0, \sin\varphi]$ into (2):

$$\alpha[\varphi] = \alpha_{33} + \cos^2\varphi\,(\alpha_{11} - \alpha_{33}), \tag{3}$$

$$\alpha'[\varphi] = \frac{\partial\alpha}{\partial\varphi} = -2\cos\varphi\sin\varphi\,(\alpha_{11} - \alpha_{33}), \tag{4}$$

$$\alpha''[\varphi] = \frac{\partial^2\alpha}{\partial\varphi^2} = -2\,(2\cos^2\varphi - 1)\,(\alpha_{11} - \alpha_{33}), \tag{5}$$

$$\alpha'''[\varphi] = \frac{\partial^3\alpha}{\partial\varphi^3} = 8\cos\varphi\sin\varphi\,(\alpha_{11} - \alpha_{33}), \tag{6}$$

$\alpha[\varphi]$ approaches extreme values if $\alpha'[\varphi] = 0$, i.e. for $\varphi = 90^\circ$ (the [0 0 1] direction) or for $\varphi = 0$ ([1 0 0] and any other direction perpendicular to [0 0 1]). From Eq. (3) one finds that $\alpha[\varphi]$ vanishes for $\tan\varphi = \sqrt{-\alpha_{11}/\alpha_{33}}$, i.e. for directions that draw up a cone around $\boldsymbol{c}$ with 36.1° as the half aperture. With the lattice constants given by Viebahn [1] $a_0 = 5.084$ Å, $c_0 = 10.21$ Å one obtains, that [302] of the crystallographic lattice is close (within 40′) to this cone. It must hold for sure, that in Ref. [16] not given the experimental errors for α_{11} and α_{33} do not allow a discrimination of the 36.1° direction from [302]. A rod with that axis would not change its length upon temperature fluctuations; perpendicular to the [302] axis the thermal expansion varies from $+8.80 \times 10^{-6}\,\mathrm{K}^{-1}$ to $+18.80 \times 10^{-6}\,\mathrm{K}^{-1}$.

In directions where $\alpha''[\varphi] = 0$ and $\alpha'''[\varphi] \neq 0$ the angular dependence $\alpha'[\varphi]$ approaches extreme values for $2\cos^2\varphi - 1 = 0$; e.g. for $\varphi = (2k+1)\pi/4$. In these directions high shear stresses that are proportional to $\alpha_{11} - \alpha_{33}$ (4) must be expected under the influence of nonlinear temperature gradients. As the fracture toughness K_{IC} is small for both substances, any treatment of crystals that can produce nonlinear thermal gradients has to be performed very carefully. This is especially the case for $LiSrAlF_6$, as α is here even more anisotropic than for $LiCaAlF_6$.

2.2. Hydrolysis of CrF_3

Many fluorides show a high affinity to water. Among the components of Cr : LiCAF and Cr : LiSAF this is the case for AlF_3 and, especially, for CrF_3. The hydrolysis of CrF_3 results in the

formation of chromium(III)-oxide

$$2\,CrF_3 + 3\,H_2O \rightleftarrows Cr_2O_3\downarrow + 6\,HF\uparrow \quad (7)$$

that precipitates as dark-green particles from the fluoride melt. Pinning of such particles at the solid–liquid interface of the growing crystal results in heavy damage of the boule; usually twinning can be observed in such cases. The equilibrium constant of the hydrolysis reaction (7) can be written as

$$k_p[\mathrm{atm}^3] = \frac{p_{HF}^6}{p_{H_2O}^3} \quad (8)$$

with the total pressure

$$p_t = p_{HF} + p_{H_2O} \quad (9)$$

as the sum of the partial pressures of hydrogen fluoride and water in the surrounding atmosphere. Higher T and lower p_t shift (7) to the right-hand side. The data for the equilibrium constant (8) given by Gmelin [19] can be fitted by the parameters $a = 17.2 \pm 0.2$ and $b = (-14{,}500 \pm 200)$ K joining the equation

$$\lg k_p = a + b\,\frac{1}{T}\,. \quad (10)$$

It has been shown recently [20], that the hydrolysis of chromium fluoride is almost complete at the melting temperatures of both LiSAF and LiCAF (765°C or 809°C, respectively) and atmospheric pressure.

3. Phase relations

The complete ternary phase diagrams $LiF–Me^{II}F_2–Me^{III}F_3$ (Fig. 2) were not yet investigated. For DTA results and for a more detailed discussion of the present knowledge on some existing compounds and the relevant thermodynamic properties and phase relations the reader is referred to recent papers [14,20–22]. Only features that are considered to be important for the crystal growth process are given here:

- It is usually reported, that the only ternary compound of the system melts congruently with the stoichiometry $Li : Me^{II} : Me^{III} = 1.0 : 1.0 : 1.0$. At least for $Me^{II} = Ca$ and $Me^{III} = Al$ this assumption is disputatious, as the eutectic composition of the binary system Li_3AlF_6/CaF_2 (solid line) contains less CaF_2 than the intersection with the conode $LiF/LiCaAlF_6$ (dashed line from the left).
- In contradiction to LiSAF, the DTA melting curve of LiCAF shows a shoulder, thus indicating incongruent melting behavior. It should be remarked, that LiSAF is usually reported to show better optical quality than LiCAF.
- DTA measurements with compositions on the binary section $LiAlF_4/CaF_2$ (vertical dashed line) showed a maximum of the liquidus for the composition $(LiAlF_4)_{0.52}\cdot(CaF_2)_{0.48} = LiCa_{0.92}AlF_{5.84}$. Measurements on the corresponding section within the system $LiF–SrF_2–AlF_3$ showed no significant deviation from the $LiAlF_4 : SrF_2 = 1 : 1$ stoichiometry.
- An accurate determination of the occupation factors by X-ray structure analysis is not possible for the Li atoms, as this light element has a too small scattering amplitude. Neutron powder diffraction data refinement for $LiCaCrF_6$ [23] results in the following occupational factors: $n_{Li} = 1.99 \pm 0.07$, $n_{Ca} = 1.90 \pm 0.05$, $n_{Cr} = 2.00$ (held fixed), $n_F = 11.85 \pm 0.18$. (2 formula units per unit cell, $P\bar{3}1c$.) The corresponding chemical composition is $(LiCrF_4)_{0.513}\cdot(CaF_2)_{0.487} = LiCa_{0.95}CrF_{5.90}$.

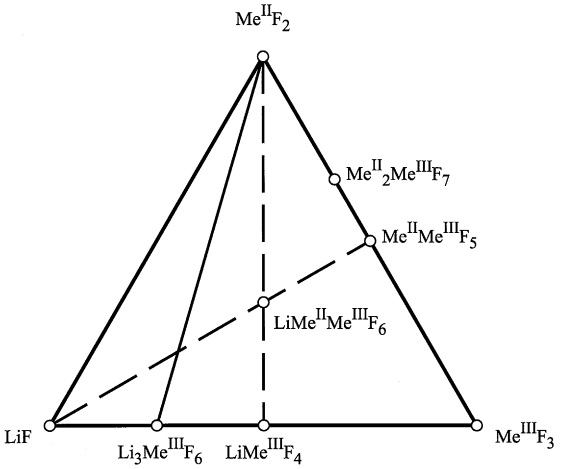

Fig. 2. Concentration triangle $LiF – Me^{II}F_2 – Me^{III}F_3$ with the existing binary compounds and the only 1 : 1 : 1 ternary compound.

From these data it must be concluded, that both $LiCaAlF_6$ and $LiCaCrF_6$ are crystallizing with a CaF_2 deficiency of $\gtrsim 5\%$. The existence range of solid $LiCaAlF_6$ is expected to be considerably broader towards CaF_2 near the melting temperature. The occurrence of Ca-rich scattering centers within the crystals can be explained by precipitation due to the narrowing existence range during the cooling process.

4. Experimental procedure

4.1. Thermal analysis and MS of the fluorides

The moisture content of the raw material and of the growth atmosphere influences heavily the quality of the pulled fluoride crystals. The manufacturers are usually sealing commercial anhydrous CrF_3 into ampoules under argon atmosphere. The purity of the substance (best 4N) is given on "metals basis"; accordingly no data about the partial substitution of fluoride ions by OH^- and/or O^{2-} are available. However, a semi-quantitative characterization of CrF_3 in terms of moisture content could be obtained by thermoanalytic measurements (DTA) and a combined mass spectrometric (MS) analysis of the emanating gaseous species.

Different CrF_3 samples (supplier AAPL, each sample ≈ 70 mg) were heated with 10 K/min in Pt-95%/Au-5% crucibles using a NETZSCH STA 409C thermoanalytic equipment. During the DTA measurements a permanent analysis of the emanating gas was performed with a BALZERS quadrupole mass spectrometer. A two-step carbon aperture ("skimmer") system performed the pressure reduction from the initial atmospheric pressure around the sample via a tuned intermediate vacuum (1–10 mbar) to the stabilized high vacuum within the MS (1×10^{-5} mbar). NETZSCH recommends the application of Ar gas for rinsing both furnace and sample. Unfortunately, the 2 most dominant of the 3 isotopes of natural argon ($^{36}Ar = 0.34\%$, $^{38}Ar = 0.06\%$, $^{40}Ar = 99.60\%$) were disturbing the detection of both water

$$m/z\,[H_2O^+] = m/z\,[^{36}Ar^{2+}] = 18 \quad (11)$$

and hydrogen fluoride

$$m/z\,[HF^+] = m/z\,[^{40}Ar^{2+}] = 20 \quad (12)$$

that were expected to be present in the emanating gas due to simple desorption of humidity or due to the reaction of water with CrF_3 (7). Accordingly, the sample was rinsed instead by He of atmospheric pressure. The ion currents resulting in the MS SEM multiplier for $m/z = 18 \Rightarrow H_2O$ (11) and for $m/z = 20 \Rightarrow HF$ (12) are shown in Fig. 3.

For all 3 measurements the same nominally anhydrous 4N CrF_3 starting material (supplier AAPL) was used. The "as delivered" sample (circles) shows moderate HF and H_2O signals up to $T = 800$–$900^\circ C$. The drop of the H_2O signal near $700^\circ C$ is related to the chemical equilibrium of the water traces with the skimmer material (carbon), $H_2O + C \rightleftharpoons H_2 + CO$, that consumes water. In the whole T range of the measurement the HF signal is slightly and the H_2O signal is even

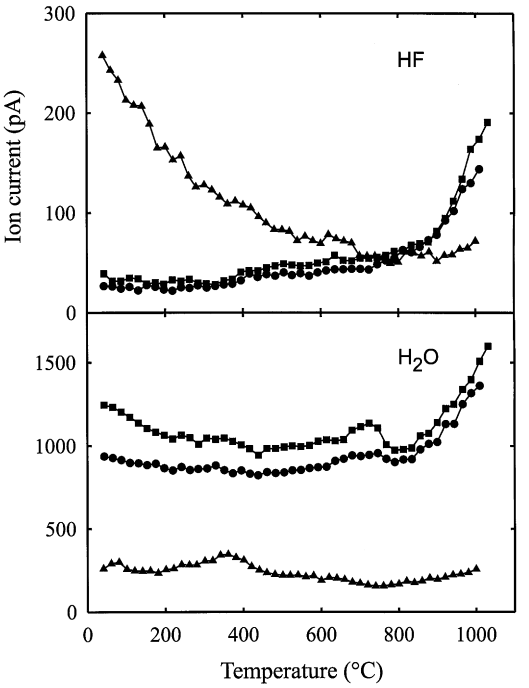

Fig. 3. Ion current (MS data) of the species $m/z = 20$ (HF, top) and $m/z = 18$ (H_2O, bottom) over different CrF_3 samples: (●) CrF_3 AAPL 99.99%; (■) CrF_3 AAPL 99.99%, 3 days exposed to air; (▲) CrF_3 AAPL 99.99% after F_2 treatment.

significantly increased, if the same CrF_3 material was stored at the room air for 3 days prior to the measurement (squares).

A reduced H_2O signal could be observed for CrF_3 that was treated with elementary fluorine at elevated T ($\approx 300^\circ C$). The resulting H_2O signal (triangles in Fig. 3 bottom) is nearly constant for all T and only $\frac{1}{3}$ as high as for the non-fluoridated sample. The drastically increased HF signal of the fluoridated sample is remarkable. In contrast to the untreated material and to the CrF_3 that was exposed to air, this very high signal for $m/z = 20$ drops upon heating continuously. It can be assumed, that F_2 destroys at least partially the moisture content of the CrF_3 according to

$$H_2O + F_2 \rightarrow 2\,HF + \tfrac{1}{2}\,O_2 \qquad (13)$$

and leads to the transformation of adsorbed water into partially adsorbed hydrogen fluoride. The high polarity of the HF molecule and the strong hydrogen bond of the hydrogen fluoride ion $[F^{\ominus}\text{–}H^{\oplus}\text{–}F^{\ominus}]^-$ (110 kJ/mol) are expected to enable strong adsorptive binding forces to the CrF_3 surface that break at a higher T. This high binding energy stabilizes bulk hydrogen fluorides as $KF \cdot HF$ and $NH_4F \cdot HF$ up to $\simeq 200^\circ C$.

Some authors propose the addition of ammonium hydrofluoride, $NH_4F \cdot HF$, to the starting material for the growth of fluoride crystals. The decomposition of this substance according to

$$NH_4F \cdot HF \rightarrow NH_3\uparrow + 2\,HF\uparrow \qquad (14)$$

is expected to shift the equilibrium (7) to the left-hand side. It was found, however, that such treatment does not improve the quality of the crystals. Impurities may be introduced into the starting material, as commercially available $NH_4F \cdot HF$ is usually of very crude purity of typically 95%. (Recently offered high-purity $NH_4F \cdot HF$ (e.g. ALDRICH #45,583-0 [24]) was not available at the time of this study.)

The decomposition of $NH_4F \cdot HF$ starts already at 120°C and is finished with the complete evaporation at (depending from the heating rate) $T \gtrsim 200^\circ C$. Fig. 4 shows a simultaneous TG/MS measurement of the substance in helium atmosphere. The mass loss starts with the emission of ammonia. This process is accompanied by a sharp

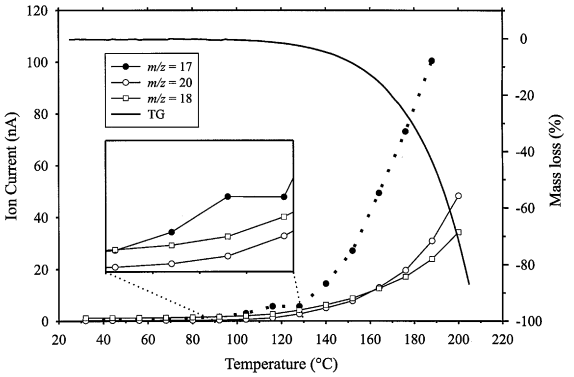

Fig. 4. Thermogravimetric (TG) measurement and simultaneous MS data for $m/z = 17$ ($[NH_3]^+$, filled circles), $m/z = 20$ ($[HF]^+$, hollow circles) and $m/z = 18$ ($[H_2O]^+$, hollow squares) of 9.76 mg $NH_4F \cdot HF$ in Pt/Au crucibles (heating rate 10 K/min). Inset: MS data for $T = 90$–$130^\circ C$.

endothermic DTA peak (not shown in the figure) ranging from 120–130°C and by shoulders in the MS(T) curves for $m/z = 15$ ($[NH]^+$), $m/z = 16$ ($[NH_2]^+$) and $m/z = 17$ ($[NH_3]^+$). Both $m/z = 16$ (relative intensity 80%) and $m/z = 15$ (relative intensity 8%) are accompanying the main peak of ammonia $m/z = 17$ (100%). The concentration of HF with $m/z = 20$ rises continuously until the whole substance is evaporated. As the purity of the $NH_4F \cdot HF$ is expected to be not better than 95–98%, it must be assumed, that it is contaminated with different substances, among them water. The significant signal $m/z = 18$ is obviously related to that water. One could argue, that $m/z = 18$ might be due to ammonium ions $[NH_4]^+$, but if that should be the case, the curve would show the same shoulder as $m/z = 15$–17 which is not the case.

In another experiment CrF_3 was treated with HF gas in the same manner as with F_2. In contrast to the reduced H_2O signal of the fluoridated sample (cf. Fig. 3) this hydrofluorided material did not show MS signals that were significantly different from the untreated sample. The oxidation of adsorbed water to oxygen according to Eq. (13) seems to be much more efficient than the shift of the equilibrium (7) to the left-hand side by an excess of HF.

4.2. Thermal analysis of the $LiF–CaF_2–AlF_3$ system

DTA results obtained on the section $LiAlF_4–CaF_2$ have been reported recently [22]. In the present work we report on new results that were obtained on the binary section $LiF–CaAlF_5$. The latter compound is one of the two binary Ca–Al fluorides and melts incongruently [25]. Vrbenská and Malinovský found the system $LiF–Li_3AlF_6–CaF_2$ to be simple eutectic [26]. The binary section $LiF–CaAlF_5$ crosses partially this well investigated ternary system. As the compound $LiCaAlF_6$ lies outside (Fig. 2) it was not reported in this formed study. Compositions ranging from $x_{CaAlF_5} = 0$ (LiF) to $x_{CaAlF_5} = 0.4$ (marked by the dashed line in Fig. 5) match the range that was already reported by Vrbenská and Malinovský.

The temperature of the ternary eutectic found in this concentration range ($T_{eut} = 667°C$) matches well the eutectic temperature that was reported in the former study [26] ($T_{eut}^{Vrb.} = 665°C$). However, it is surprising, that the investigated section is not really binary. Besides the 667°C peak and the liquidus peak the DTA curves showed a third peak at intermediate temperatures. Such behavior is typical for real ternary systems and confirms the proposition, that the composition of LiCAF deviates from the ideal $Li : Ca : Al = 1 : 1 : 1$ stoichiometry. Accordingly, the section $LiF–CaAlF_5$ is even in the concentration range between $LiF–LiCaAlF_6$ not really binary.

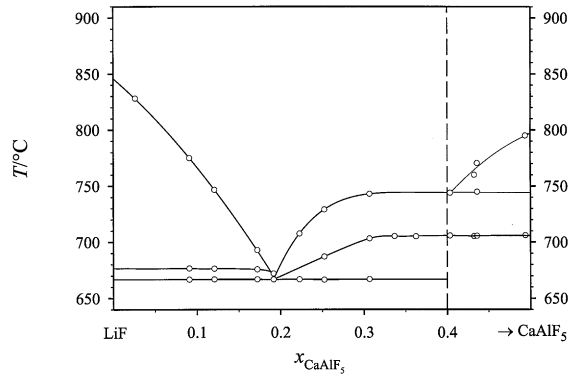

Fig. 5. Binary section $LiF–CaAlF_5$ as obtained by DTA measurements. $x_{CaAlF_5} = 0.5$ corresponds to the composition of stoichiometric $LiCaAlF_6$.

Right from the dashed line in Fig. 5, and thus outside the partial system $LiF–Li_3AlF_6–CaF_2$, the liquidus temperature rises until it reaches the melting point of LiCAF. The maximum liquidus temperature found in this study (801°C) is about 9 K below the value that was obtained in a previous study [22]; but it should be kept in mind, that the quasi-binary section in the present study does not cross the composition of the liquidus maximum that was found to occur at the composition $LiCa_{0.92}AlF_{5.84}$ (Section 3). The part of the quasi-binary section right from $LiCaAlF_6$ ($x_{CaAlF_5} > 0.5$) could be explained not sufficiently with the current data. In this concentration range the melts solidify to become partially vitreous — this circumstance hinders the interpretation of DTA curves drastically.

4.3. Growth of single crystals

The growth of colquiriite-type crystals starts from stoichiometric or nearly stoichiometric melts and has been reported by different methods. Usually Czochralski [16] or Bridgman pulling [11] are applied. In this study LiCAF and LiSAF single crystals were grown exclusively by the Czochralski method with RF heating and automated diameter control. Powdered LiF, CaF_2 (or SrF_2, respectively), AlF_3 (each GFI, 4N) and CrF_3 (AAPL, 4N) were used as starting material. The growth chamber was rinsed by 5N nitrogen (< 2 ppm H_2O) to reduce hydrolysis of the fluorides as far as possible. The handling of the starting materials (charging and pre-melting in the platinum or vitreous carbon crucible) was performed in a nitrogen rinsed glove box too. A part of the remaining adsorbed water can be removed from the surface of the starting materials, if the powders are slowly heated to $\approx 300°C$ in vacuum.

A rotation rate of 15–20 rpm proved to be suitable for pulling the crystals with 18 mm diameter from crucibles with 40 mm diameter and 40 mm height. (For crystals with up to 30 mm diameter the rotation rate had to be decreased and the crucible diameter and height was kept about twice the diameter of the boule.) The cylindrical part of the boule has usually slightly elliptical cross section; the ellipticity increases with increasing rotation

rate. The basal plane (0 0 0 1) perpendicular to the trigonal axis of the crystal is facetted.

Problems upon diameter control may arise, as the fluoride (especially LiSAF) melts wet the Pt crucible highly. Fluctuations of this wetting height lead to uncontrollable fluctuations of the mass signal at the diameter control system and thus to growth rate and diameter fluctuations. Similar observations were reported by Chai et al. in a previous paper [27]. Volatile LiF/AlF_3 evaporates especially from the thin wetting layer that creeps along the crucible wall; thus leading to a stoichiometry shift of the melt. The surface tension of the melt layer at the crucible wall is expected to be dependent on the composition. If the layer thickness changes due to changing surface tension, fluctuations of the melt height within the crucible and thus the observed fluctuations of the mass signal may occur. Vitreous carbon crucibles are less wetted by the melt, but lead, unfortunately, quite often to the formation of carbon particles.

Fig. 6 presents the results of temperature measurements in the set-ups that were used for the growth of LiSAF (full squares, without active afterheater) or LiCAF single crystals (empty squares, with active afterheater), respectively. The temperature measurements were performed in the original set-up, but without crystal and with an empty crucible. It must hold for sure, that the actual $\partial T/\partial z$ during the growth process is different from the date given in Fig. 6, but at least the tendency should remain the same during the pulling process. (The actual melt temperature is for LiSAF about 40 K higher than the maximum temperature of the plot.) The gradients given in the figure result from a linear fit of $T(z)$ for $z = 30$–40 mm that is marked by two dashed lines. The melt surface during crystal growth is initially at $z = 35$ mm in the middle between both dashed lines.

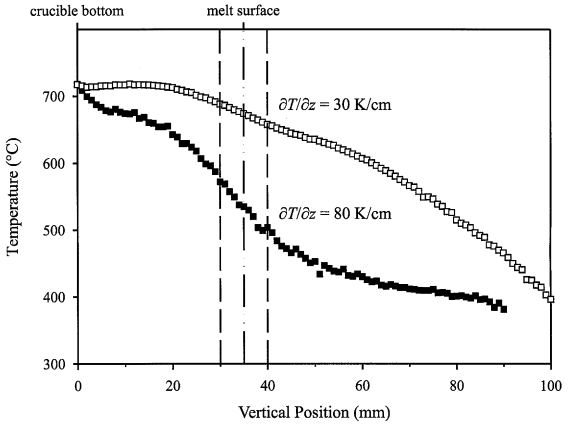

Fig. 6. Temperature T versus vertical position z within the Czochralski setup as measured without crystal: (■) $T(z)$ without active afterheater for LiSAF growth; (□) $T(z)$ with active afterheater for LiCAF growth.

The very high (some hundreds K/cm) temperature gradients $\partial T/\partial z = G_T$ (z — vertical coordinate) that are typical for RF heating were reduced by passive afterheaters to about 80 K/cm. An even more effective adjustment of G_T could be obtained by active afterheaters that were described elsewhere in more detail [28]. In this case a second RF coil is placed around a platinum cylinder surrounding the boule during crystal growth. Moreover, a substantial better adjustment of G_T is possible due to the separate regulation of the RF power that is produced by the afterheater coil. If G_T is too high, the following problems may occur:

- Due to the high anisotropy of ${}^2\tilde{\boldsymbol{\alpha}}$ (cf. Section 2) the crystal may crack. It proved to be difficult to grow LiSAF with diameters of > 10 mm, as anisotropy ratios

$$R_\alpha = \frac{|\alpha_{11} - \alpha_{33}|}{\frac{1}{2}(\alpha_{11} + \alpha_{33})},$$

  where $R_\alpha = 1.4$ for LiCAF and $R_\alpha = 6.5$ for LiSAF, respectively, result from the data given in Table 1. Thermal cracking occurs parallel $(0\,1\,\bar{1}\,0)$ and perpendicular to the basal plane (0 0 0 1). As the growth direction $\boldsymbol{a} = [2\,\bar{1}\,\bar{1}\,0] = [1\,0\,0]$ lies within the cleavage plane, the boules crack into two parts of nearly equal size. The production of laser rods with 3–7 mm diameter and up to 100 mm length is possible from both parts.
- The overheating of the crucible must be increased, if high G_T are applied. Due to the high volatility of $LiAlF_4$ [20] the stoichiometry of the melt may shift. This is especially the case for the growth of LiCAF, as the melting temperature of this substance is 44 K higher than the melting temperature of LiSAF.

The flat G_T applied during LiCAF growth is assumed to perform an "in situ" annealing procedure that is known to improve crystal quality [29]. On the other side, it is more difficult to avoid constitutional supercooling under low gradient conditions. It was found, that the growth of single crystals with diameters > 18 mm is easier for LiCAF. On the other side, the light scattering losses with typically up to 2%/cm for such crystals are about one order of magnitude higher than that for LiSAF crystals. The growth of high quality (scattering loss < 0.2%/cm) LiCAF crystals with diameters < 10 mm too, is possible if a pulling rate < 1 mm/h is applied.

4.4. Electron microscopy and electron diffraction

Electron diffraction experiments were performed in order to identify the phase composition of the solidified melt after DTA characterization using a transmission electron microscope JEOL JEM 750D. The examined DTA specimen had a starting composition $LiF : CaF_2 : AlF_3 = 0.25 : 0.50 : 0.25$.

In order to achieve electron transparency, a piece of the solidified DTA melt was pulverized. The specimen powder was suspended in H_2O and deposited on several carbon-foil grids. Different specimens of the same solidified DTA melt were prepared and systematically examined by electron diffraction to statistically ensure the evaluation of the data. The pattern diagrams obtained by transmission high-energy electron diffraction (THEED) were photographically documented at a camera length of 1 m and an acceleration voltage of 1000 kV. The accuracy of the camera constant was calibrated using polycrystalline Au deposited on a carbon-coated grid.

Several electron diffraction diagrams were taken showing significant spot distances and remarkable symmetry configurations (Fig. 7). For the evaluation of electron diffraction diagrams, the data of all compounds were considered which are known to exist within the phase diagram $LiF–CaF_2–AlF_3$ or of those which are oxides of the involved elements. The following phases have been identified: CaF_2, $CaAlF_5$, Ca_2AlF_7, $LiCaAlF_6$, Li_3AlF_6, and CaO.

For the discussion of the results one should consider that $CaAlF_5$ and Ca_2AlF_7, as well as the "g-" and the "b-" phases of Li_3AlF_6 have similar lattice distances, respectively. Therefore, similar electron diffraction patterns have to be expected and the distinction of these phases is sometimes not sure.

As expected, $LiCaAlF_6$ proved to be the main component of the Ca-rich sample. A part of the CaF_2 excess was found to shape the binary Ca–Al fluorides. Surprisingly, CaO (Fig. 7b, NaCl structure) was found to be present in remarkable amounts. The formation of that CaO during the THEED sample preparation is unlikely, as on the one side the reaction rate of LiCAF with water is slow and on the other side the reaction of fluorides

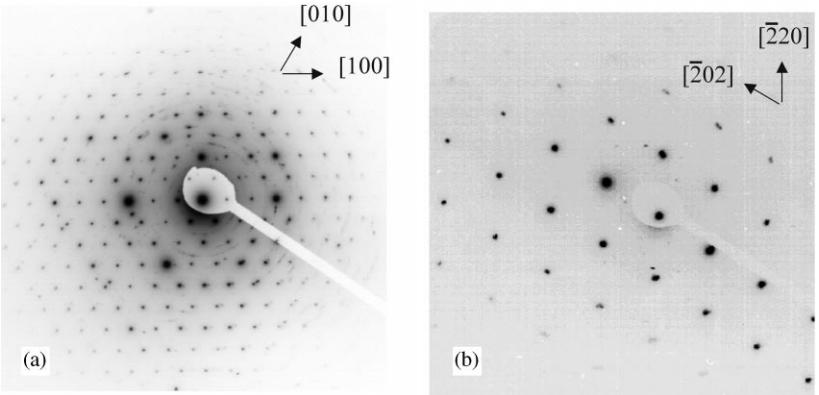

Fig. 7. Electron diffraction diagrams of particles found within a pulverized DTA sample. (a) $LiCaAlF_6$ in [0 0 1] direction, (b) CaO in $\langle 1\,1\,1 \rangle$.

with water leads to the formation of hydroxides that are stable up to $\approx 700^{\circ}C$. Any traces of hydroxides could not be found.

The presence of CaO within the Ca-rich DTA sample can be explained by partial hydrolysis of fluorides with adsorbed water. Melt temperatures up to 850°C were obtained in this concentration region during the DTA runs. Such high temperatures are known to calcine the hydroxides nearly quantitatively to the oxides. CaO was found alone, as (a) Ca is the main cation within the sample and (b) Ca is the heaviest cation with the highest scattering amplitude and (c) CaO is the only cubic oxide and has therefore a limited number of strong reflexes.

5. Discussion and summary

Undoped and Cr^{3+} doped $LiCaAlF_6$ and $LiSrAlF_6$ crystals were grown by the Czochralski technique. Scattering losses below 0.2%/cm can be obtained for both crystals. Scattering centers that are typical for LiCAF can be avoided, if slow pulling rates ≈ 0.5 mm/h and flat temperature gradients are applied. LiSAF can be grown with pulling rates of ≈ 1 mm/h and with steeper gradients. In this case the main problem is the high anisotropic thermal expansion coefficient of this crystal that easily leads to thermal cracking along $(0\,1\,\bar{1}\,0)$.

These different optimal growth conditions for both crystal are due to their substantial different thermodynamic and physical properties. In contrast to LiSAF, for LiCAF already slight deviations of the melt composition towards higher CaF_2 concentrations may lead to the incorporation of CaF_2-rich foreign phases within the crystal. Unfortunately, the liquidus of the section $LiF–CaAlF_5$ could not be detected clearly for $x_{CaAlF_5} > 0.5$ to explain these problems in detail.

Upon annealing or, alternatively, very slow pulling rates $\ll 1$ mm/h equilibration of the concentration gradients can be obtained; thus leading to a satisfactory optical quality across the whole diameter of the boule. The diffusing species could be either Ca^{2+}/Al^{3+} from the core outside (indeed, the Ca^{2+} concentration was found to vary across striations); or Li^{+} from outside towards the core.

A general problem upon the growth of high-quality fluoride crystals for optical applications arises from their sensitivity of water. The use of high-quality starting materials and the preparation under dry conditions is a necessary but not always sufficient preposition. In some cases, treatment in reactive gases or at least the partial desorption of adsorbed water by heating under vacuum conditions is suggested.

Acknowledgements

We gratefully acknowledge access to the HVEM of the Max-Planck-Institute of Microstructure Physics Halle in co-operation with Dr. U. Richter, Labor für Elektronenmikroskopie in Naturwissenschaften und Medizin Halle. The treatment of CrF_3 with HF and F_2 was performed in the laboratory of Prof. E. Kemnitz, Humboldt-Universität Berlin. One of us (D.K.) acknowledges support from the Alexander von Humboldt Foundation, Bonn. This work was supported by the BMBF (grant 624-4013-13N6750/2).

References

[1] W. Viebahn, Z. Anorg. Allg. Chem. 386 (1971) 335.
[2] K. Walenta, B. Lehmann, M. Zwiener, Tschermaks Mineralog. Petrog. Mitt. 27 (1980) 275; also American Mineralogist 66 (1981) 879 + 1099.
[3] S.A. Payne, L.L. Chase, H.W. Newkirk, L.K. Smith, W.F. Krupke, IEEE J. Quantum Electron. 24 (1988) 2243.
[4] S.A. Payne, L.L. Chase, L.K. Smith, W.L. Kway, H.W. Newkirk, J. Appl. Phys. 66 (1989) 1051.
[5] B.H.T. Chai, J.-L. Lefaucheur, M. Stalder, M. Brass, Opt. Lett. 17 (1992) 1584.
[6] L.K. Smith, S.A. Payne, L.L. Chase, W.L. Kway, B.H. T. Chai, $LiSrGaF_6 : Cr^{3+}$ – a New Laser Material of the Colquiriite Structure, CLEO'91, 1991, pp. 388–390.
[7] A. Cassanho, H.P. Jenssen, A. Umyskov, I.A. Shcherbakov, OSA Proc. Adv. Solid-State Lasers 13 (1992) 2.
[8] F. Balembois, F. Druon, F. Falcoz, P. Georges, A. Brun, Opt. Lett. 22 (1997) 387.
[9] A. Cassanho, H. Jenssen, Laser Focus World, 1997.
[10] M. Stalder, B.H.T. Chai, M. Bass, Appl. Phys. Lett. 58 (1991) 216.
[11] D.R. Lee, H.G. Gallagher, T.P.J. Han, B. Henderson, ICCG XI, Abstracts (1995) p. 506.
[12] G. Lacayo, I. Hähnert, D. Klimm, P. Reiche, W. Neumann, Cryst. Res. Technol. 34 (1999) 1221.

[13] S. Arzt, Synchrotron radiation scattering patterns of precipitates within LiCAF single crystals gave no evidence on Ca_2AlF_7 or any other foreign phases, 1997, unpublished result.
[14] D. Klimm, K. Seiranian, P. Reiche, A. Polity, R. Krause-Rehberg, SPIE Proc. 3178 (1997) 35.
[15] B.W. Woods, S.A. Payne, J.E. Marion, R.S. Hughes, L.E. Davis, J. Opt. Soc. Am. B 8 (1991) 970.
[16] G.J. Quarles, Advances in $Cr:LiSrAlF_6$ crystal growth and laser technology, in: Novel Laser Sources and Applications, Vol. PM16, SPIE Press, 1994, pp. 86–102.
[17] Y.I. Sirotin, M.P. Shaskolskaya, Fundamentals of Crystal Physics, Mir Publishers, Moscow, 1982.
[18] P. Paufler, Physikalische Kristallographie, Akademie-Verlag, Berlin, 1986.
[19] Gmelin-Institut, Gmelins Handbuch der Anorganischen Chemie, volume Chrom, Teil B, Verlag Chemie, Weinheim/Bergstr., 1962.
[20] D. Klimm, P. Reiche, Cryst. Res. Technol. 34 (1999) 145.
[21] D. Klimm, P. Reiche, Growth of $Cr^{3+}:LiCaAlF_6$ and $Cr^{3+}:LiSrAlF_6$ Crystals by the Czochralski Technique, in: T. Sasaki (Ed.), Proceedings of International Symposium on Laser and Nonlinear Optical Materials, Singapore, 1997, pp. 284–286.
[22] D. Klimm, P. Reiche, Cryst. Res. Technol. 33 (1998) 407.
[23] B. Rupp, W.L. Kway, J. Wong, P. Rogl, P. Fischer, J. Solid State Chem. 107 (1993) 471.
[24] ALDRICH, Inorganics and Organometallics, 1998–99, Catalogue.
[25] D.F. Craig, J. Jesse, J. Brown, J. Am. Ceram Soc. 60 (1977) 396.
[26] J. Vrbenská, M. Malinovský, Chem. Zvesti 21 (1967) 818.
[27] B. Chai, J. Lefaucheur, A. Pham, V. Castillo, SPIE Proc. 1863 (1993) 25.
[28] P. Reiche, B. Hermoneit, D. Schultze, Cryst. Res. Technol. 20 (1985) 845.
[29] J.J.D. Yoreo, L.J. Atherton, D.H. Roberts, J. Crystal Growth 113 (1991) 691.